Improved thermal stability and contact of antimony film by the interlayer HfO$_2$

Junbo Xu[1] · Yifeng Hu[1,3] · Tianshu Lai[2] · Yongkang Xu[1] · Song Sun[1]

Abstract

The thermal stability was one of the primary obstacles hindering the development of phase-change memory. In this paper, Sb/HfO$_2$ multilayer phase-change films were prepared by multilayer composite method. The transition process of Sb/HfO$_2$ multilayer films from amorphous to crystalline state was studied by in-situ heating. With the decrease of the thickness of Sb layer, the crystallization temperature of Sb/HfO$_2$ increased significantly. At the same time, the data retention temperature for 10 years increased from 14 °C of pure antimony to 147 °C of Sb/HfO$_2$. The bandgap became wider and the surface became smoother. The existence of a large number of Sb microcrystals inhibited the phase transformation process. Compared with single-layer Sb film, Sb/HfO$_2$ multilayer film had smaller volume change before and after phase transformation. The results showed that the addition of HfO$_2$ interlayer significantly enhanced the amorphous thermal stability of Sb and improved the effective contact between the phase-change layer and the electrode. Sb/HfO$_2$ multilayer film was a potential phase-change film with high stability and good reliability.

1 Introduction

Phase-change memory (PCM) was a new type of nonvolatile memory based on chalcogenide film [1]. Induced by the voltage pulses with different widths and heights, the phase-change materials could be converted between crystalline (low resistance) and amorphous (high resistance) states. The essence was using electrical energy (joule heat) to achieve the storage (SET) and erasure (RESET) of information [2]. The Read of information was through measuring the change in resistance. With the development of technology, the size of PCM unit could easily be reduced due to its low operating voltage, bitwise operation, faster writing speed than flash memory, excellent fatigue characteristics, hundreds of millions of cycles, simple manufacturing process and compatible with the current mature CMOS (Complementary Metal–Oxide–Semiconductor) process [3]. In especial, the great progresses were being made on semiconductor and micro-nano fabrication technology in recent years. Besides, the research foundation of phase-change materials had been accumulated in the fields of optical storage and PCM technology. All of these resulted that PCM was replacing the traditional flash memory and having a broader application space and better development trend [4].

Phase-change material was the core of phase-change memory. As a storage medium, its performance is directly related to the quality of PCM device [5]. At present, there were many phase-change materials and different classification methods. Thereinto, most of phase-change materials were made of one, two or three of the three elements (Ge, Sb and Te) [6–8]. Ge$_2$Sb$_2$Te$_5$ system is the most mature phase-change material because of its widely use in optical storage. However, the weak amorphous thermal stability limited its further application for high density and high speed memory [9]. The literature showed that Sb phase-change material had a faster crystallization rate due to its growth-dominated crystallization mechanism [10]. However, its low phase transition temperature also leads to the instability of its amorphous state [11]. The traditional doping method could improve the thermal stability of Sb and decrease the power

✉ Yifeng Hu
  hyf@jsut.edu.cn

✉ Tianshu Lai
  stslts@mail.sysu.edu.cn

1 School of Mathematics and Physics, Jiangsu University of Technology, Changzhou 213000, China

2 State-Key Laboratory of Optoelectronic Materials and Technology, School of Physics, Sun Yat-Sen University, Guangzhou 510275, China

3 National Laboratory of Solid State Microstructures, Nanjing University, Nanjing 210093, China

consumption while slowing down the phase transition speed [12]. The multilayer composite film could improve the thermal stability and maintain low operating power consumption due to its low thermal conductivity [7, 13]. Therefore, it had received continuous attention from researchers. Hafnium dioxide (c) was a common stable oxide of hafnium. It was an insulator with a wide bandgap of 5.3 to 5.7 eV, which had both a high dielectric constant ($K - 25$) and a breakdown electric field (5 mV/cm) [14]. Therefore, it had good thermal stability. In this paper, HfO_2 was used as an interlayer material to composite with Sb through a multilayer stack. By studying its thermal, optical and electrical properties, the potential value of Sb/HfO_2 multilayer film as phase-change material is considered comprehensively.

2 Experimental

The Sb/HfO_2 multilayer films were prepared at room temperature by alternately sputtering HfO_2 and Sb targets on Si/SiO2 substrates in a radio frequency (RF) magnetron sputtering system. The targets with the purity of 99.999% were carefully cleaned to remove the impurities on the surface before sputtering. In order to ensure the temperature of substrate, the instrument was cooled by circulating water during sputtering. The background pressure of the vacuum chamber was lower than 2×10^{-5} pa with a sputtering gas pressure of 4×10^{-1}Pa. The flow rate of high-purity argon (AR) was 30 sccm (sccm was standard ML/min). The powers of Sb and HfO_2 targets were set at 30 and 60 W, respectively. The rotary speed of the substrate was 20 rpm to ensure the uniformity of deposition. The thickness of each individual layer was designed by controlling the sputtering time. The total thickness of multilayer Sb/HfO_2 and monolayer Sb thin films were set to approximately 50 nm.

The crystallization temperature of the film can be obtained by measuring the heating process of the sample in in-situ resistance temperature ($R–T$) system with a two-point-probe setup. An argon protection test chamber was introduced to prevent the oxidation of the film in the heating process. At the same time, the films were kept at different isothermal temperatures for time-dependent resistance measurement to estimate the data retention and activation energy for crystallization (E_a). The reflectivity of the film was measured by a near-infrared spectrophotometer (NIR, 7100 CRT, XINMAO, China) in the wave length range of 400–2500 nm and the bandgap was obtained by Kubelka–Munk's law. The crystalline phase structure at various temperatures was analyzed by X-ray diffraction (XRD) with Cu Ka radiation in the 2θ range from 20 to 60º performed at 40 kV and 40 mA, with a scanning step of 1° per min. The surface morphology of the film was observed by atomic force microscopy (AFM), which was aimed to analyze the change of roughness

in annealing. 50-nm-thick samples were prepared for X-ray reflectometry (XRR) measurement to estimate the density change of film during crystallization.

3 Results and discussion

The crystallization process of Sb/HfO_2 multilayer films was analyzed by in-situ resistance–temperature measurement. Figure 1 shows the $R–T$ curves of Sb monolayer thin films and Sb/HfO_2 multilayer composite films measured at a fixed heating rate of 30 °C/min. It could be seen from Fig. 1 that the resistances of all films decreased slowly at first from high resistance, which was called the nucleation stage. When the temperature reached a specific value, the resistance decreased rapidly. This temperature was defined as the crystallization temperature T_c[15]. After T_c, the phase transformation process changed from nucleation to growth. The resistance ratio between amorphous and crystalline states for Sb/HfO_2 was over two orders of magnitude, which could meet the requirement of PCM. Figure 1 shows that the T_c for [Sb(18 nm)/HfO_2(1 nm)]$_3$, [Sb(14 nm)/HfO_2(1 nm)]$_3$, [Sb(12 nm)/HfO_2(1 nm)]$_4$, [Sb(11 nm)/HfO2(1 nm)]$_4$, [Sb(10 nm)/HfO_2(1 nm)]$_5$ and Sb films were 188, 209, 224, 231, 239 and 154 °C, respectively. Generally, the thermal stability could be evaluated by the crystallization temperature roughly. It revealed that the thermal stability of the Sb/HfO_2 multilayer composite films was improved as a whole compared with the monolayer Sb film [16]. Moreover, the crystallization temperature of Sb/HfO_2 composite films was higher than that of GST ($- 160$ °C) [17]. The key issue of GST in commercial application was its relatively low crystallization temperature, which resulted in poor thermal stability. Furthermore, the crystalline resistances of Sb/HfO_2
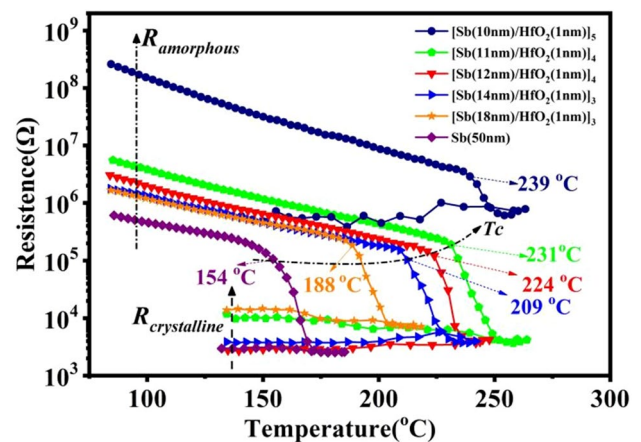

Fig. 1 Resistance as a function of temperature for Sb/HfO_2 multilayer composite thin films with different thickness ratios at a heating rate of 30 °C/min

thin films increased with the decrease of period thickness of Sb layer. Thus, Sb/HfO$_2$ multilayer thin films also had better thermal stability than Sb.

Beyond T_c, the resistances of all films maintained in low and stable values, indicating the formation of crystallization states and turning into coarsening stage. Furthermore, the crystalline resistances of Sb/HfO$_2$ thin films gradually increased with the decrease of the thickness of Sb layer. A better self-heating efficiency could be achieved with a higher resistance according to the joule heat $Q = I^2 \times R \times t$ [18], where Q, I, R, t were joule heat, current, resistance and time, respectively. It could reduce the pulse current of the Joule heating and contribute to reduce the power consumption in the RESET process. In addition, the resistance difference of pure Sb film before and after crystallization was smaller than that of Sb/HfO$_2$ thin films. It might be ascribed to the partial crystallization of Sb during the deposition process due to its poor amorphous thermal stability. After compositing with HfO$_2$, the resistance difference became larger, which was conducive to keep an enough SNR (Signal-to-Noise Ratio) for PCM device [19].

Good thermal stability of the phase-change materials was beneficial to and reliability of PCM devices. In this work, the crystallization method was applied to evaluate the data retention. Figure 2a–c shows the normalized resistance as a function of annealing time at various isothermal temperatures for [Sb(10 nm)/HfO$_2$(1 nm)]$_5$, [Sb(14 nm)/HfO$_2$(1 nm)]$_3$ and [Sb(20 nm)/HfO$_2$(1 nm)]$_3$ thin films. A lower isothermal temperature corresponded to a longer incubation period. The failure time was defined as the time when the resistance dropped to half of its initial value at isothermal temperatures [17]. Figure 2a reveals that the failure time of [Sb(10 nm)/HfO$_2$(1 nm)]$_5$ thin film at the annealing temperature 234, 224 and 219 °C were 33, 212 and 397 s, respectively. Similarly, the failure time for [Sb(10 nm)/HfO$_2$(1 nm)]$_5$ film increased from 66 s of 204 °C to 1320 s of 189 °C. According to the same test method, the failure time of other films was also measured (not shown here). The similar tendency could be obtained for all other Sb/HfO$_2$ thin films. As was known, the phase-change film needed more time to accumulate the energy for the nucleation and grain growth in a lower isothermal temperature [20]. Figure 2d is obtained by fitting failure time vs. isothermal temperature of different films linearly.

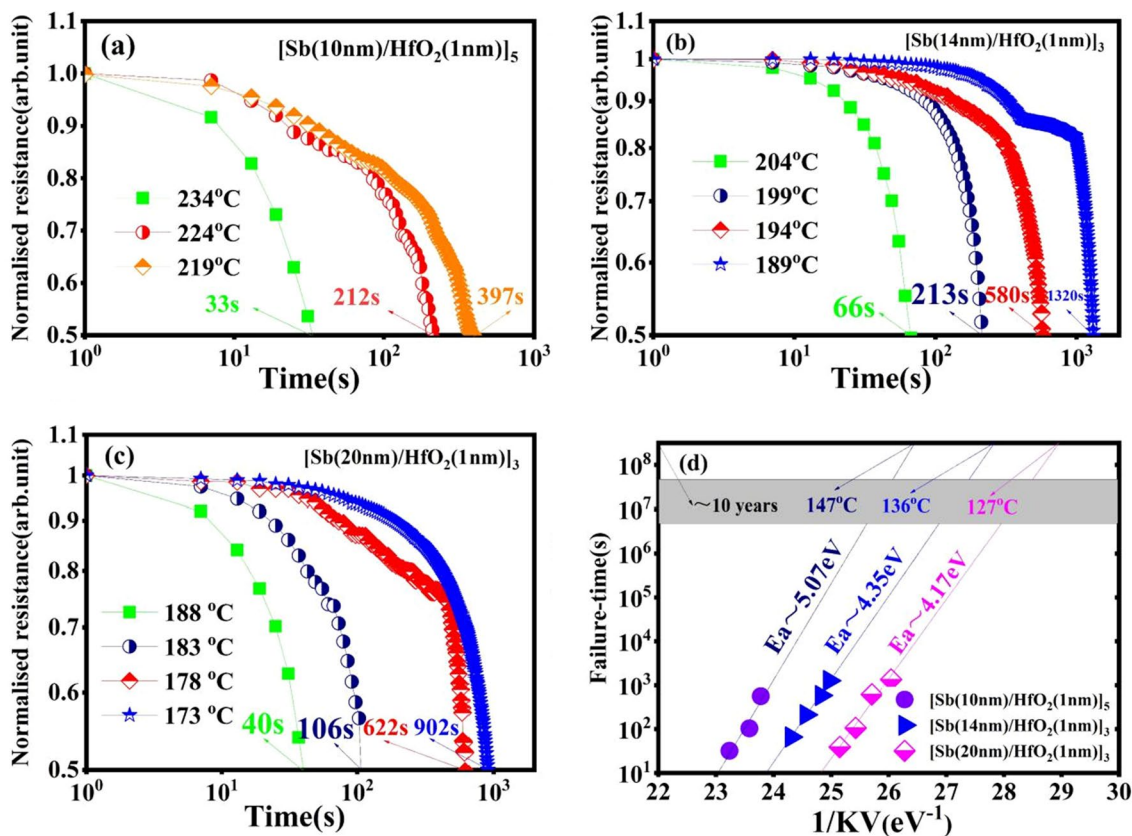The activation energy E_a was another significant index for assessing thermal stability. A larger E_a meant a greater

Fig. 2 **a–c** The change of normalized resistance with time for [Sb($a$nm)/HfO2(1 nm)]5 (a = 10, 14, 20) thin films at isothermal annealing process; **d** is the plot of failure time versus reciprocal temperature, showing the data retention temperature for 10 years and Arrhenius plots for E_a

crystallization obstacle. The temperature for 10-year data retention could be obtained from the extrapolated fitting curve based on the Arrhenius equation. The Arrhenius equation showed the relationship between failure time and activation energy [21]:

$$t = \tau \exp(E_a/kT), \tag{1}$$

where t, τ, E_a, k and T were failure time, the pre-exponential factor depending on the material's properties, the activation energy of crystallization, Boltzmann's constant and absolute temperature of concern, respectively. Figure 2d shows the fitting result of a plot of failure time versus $1/(kT)$. As shown in Fig. 2d, the E_a of [Sb(10 nm)/HfO$_2$(1 nm)]$_5$, [Sb(14 nm)/HfO$_2$(1 nm)]$_3$ and [Sb(20 nm)/HfO$_2$(1 nm)]$_3$ were 5.07, 4.35 and 4.17 eV, respectively. By contrast, the E_a of pure Sb thin film was only 1.27 eV [22], which indicated that there was a greater crystallization barrier to restrain the crystallization of Sb/HfO$_2$ multilayer films. Besides, the data retention temperatures for 10 years of [Sb(10 nm)/HfO$_2$(1 nm)]$_5$, [Sb(14 nm)/HfO$_2$(1 nm)]$_3$ and [Sb(20 nm)/HfO$_2$(1 nm)]$_3$ thin films were 147, 136 and 127 °C, respectively, which were much higher than that of GST (− 85 °C) and pure Sb thin film (− 14 °C) [22]. Compared with GST, Sb/HfO$_2$ multilayer films was more appropriate for high-temperature PCM application, and was selected to investigate its further application for PCM cell. It revealed that the data retention ability was greatly enhanced with the decrease of the thickness of Sb layer in Sb/HfO$_2$ multilayer films. From this perspective, Sb/HfO$_2$ thin films possessed better reliability of the amorphous state to meet the application of data storage at elevated temperature.

The reflectivity spectra of Sb and Sb/HfO$_2$ films were measured by UV–VIS–NIR spectrophotometry in the wavelength range of 400 to 2500 nm at room temperature. Fi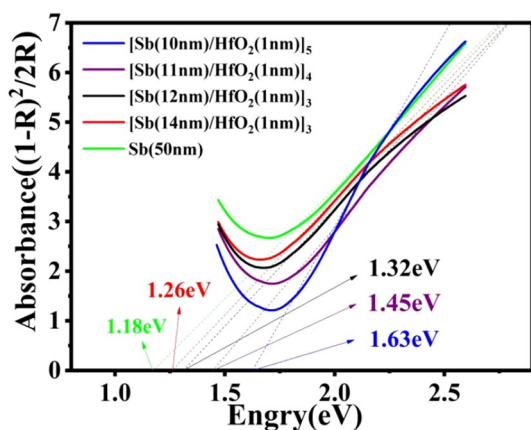gure 3 shows the plot of the absorbance vs. energy of monolayer Sb and multilayer Sb/HfO$_2$ thin films. The Kubelka–Munk function (K–M) was as follows, which was used to obtain the conversion of reflectivity to absorbance data [23].

$$K/S = (1 - R^2)/(2R), \tag{2}$$

where R was the reflectivity, K was the absorption coefficient and S was the scattering coefficient. When free electrons absorbed enough energy, they could jump from valence band to conduction band. The width between valence band and conduction band was the forbidden band. As shown in Fig. 3, the bandgap energy Eg for Sb, [Sb(10 nm)/HfO$_2$(1 nm)]$_5$, [Sb(11 nm)/HfO2(1 nm)]$_4$, [Sb(12 nm)/HfO$_2$(1 nm)]$_4$ and [Sb(14nm)/HfO$_2$(1 nm)]$_3$ were 1.18, 1.63, 1.45, 1.32 and 1.26 eV, respectively. Compared with the amorphous Sb thin film, the amorphous Sb/HfO$_2$ thin films had a wider bandgap. Besides, with the decrease of Sb period thickness, the Eg of Sb/HfO$_2$ amorphous films became bigger, which indicated that the thermal stability of amorphous state was enhanced. In general, the carrier concentration inside the semiconductors was proportional to $\exp(-Eg/2kT)$ [24]. An increase in the bandgap would lead to the decrease of carriers, which made a major contribution to the increase of resistivity for amorphous film. This finding was in accordance with the result of R–T curves in Fig. 1.

The crystallization behavior of [Sb(11 nm)/HfO2(1 nm)]$_4$ thin film was examined by XRD patterns. Figure 4 shows the XRD patterns of the materials after annealing at different temperatures for 22 min. No diffraction peaks were observed in the as-deposited and 170 °C annealed [Sb(11 nm)/HfO2(1 nm)]$_4$ thin films, indicating an amorphous nature. With the increase of annealing temperature to 231 °C, the obvious diffraction peak of (003), (012) and (006) began to appear, which belonged to Sb phase [25]. It indicated
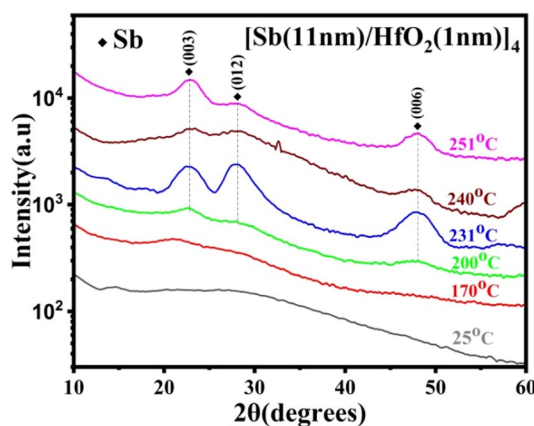
Fig. 3 The Kubelka–Munk function of monolayer Sb and multilayer Sb/HfO$_2$ thin films

Fig. 4 XRD patterns of [Sb(11 nm)/HfO2(1 nm)]$_4$ multilayer thin films annealed at different temperatures for 22 min in Ar atmosphere

that the crystallization had occurred in the material. With the further increase of annealing temperature to 240 and 251 °C, these Sb diffraction peaks continued to exist. Pure Sb material had been proved to have ultrafast phase-change speed due to its growth-dominated crystallization mode [26]. The existence of a large number of Sb phases in [Sb(11 nm)/HfO2(1 nm)]$_4$ thin film could quicken the crystallization process and reduce the operation power consumption. Besides, no diffraction peaks belonging to HfO$_2$ were observed in the XRD curves, indicating the existence of HfO$_2$ in amorphous state. The crystallization of Sb in Sb/HfO$_2$ materials was restrained by amorphous HfO$_2$ layers due to the holding effect of interfaces in the [Sb(11 nm)/HfO2(1 nm)]$_4$ multilayer thin films. It was conducive to improve the stability of Sb materials. The HfO$_2$ interlayers played an important role in improving the crystallization temperature and the thermal stability of Sb films, which was beneficial to the reliability of the PCM device. We could calculate the grain size of multilayers by using the Scherrer equation [27]:

$$D_{hkl} = 0.943\lambda/(\beta cos\theta), \qquad (3)$$

where D_{hkl} was Grain size, λ was wavelength of the X-ray (0.154 nm), β was the full-width at-half-maximum (FWHM), and θ was the diffraction angle. The average grain size of [Sb(11 nm)/HfO2(1 nm)]$_4$ was 5.2 nm, which belonged to microcrystalline. Moreover, it was much less than that of GST (40.3 nm) [28]. The small microcrystalline further proved that the crystallization was inhibited, resulting in more crystal boundaries and a higher resistance. This was beneficial to decrease the volume change before and after crystallization and improve the reliability of PCM device.

The surface roughness of film was of great significance for the device performance by influencing the quality of the electrode-film interface during the phase-change process. The change of surface morphology of the film was related to the internal stress [29]. Figure 5 shows the evolution of surface images for the multilayer [Sb(11 nm)/
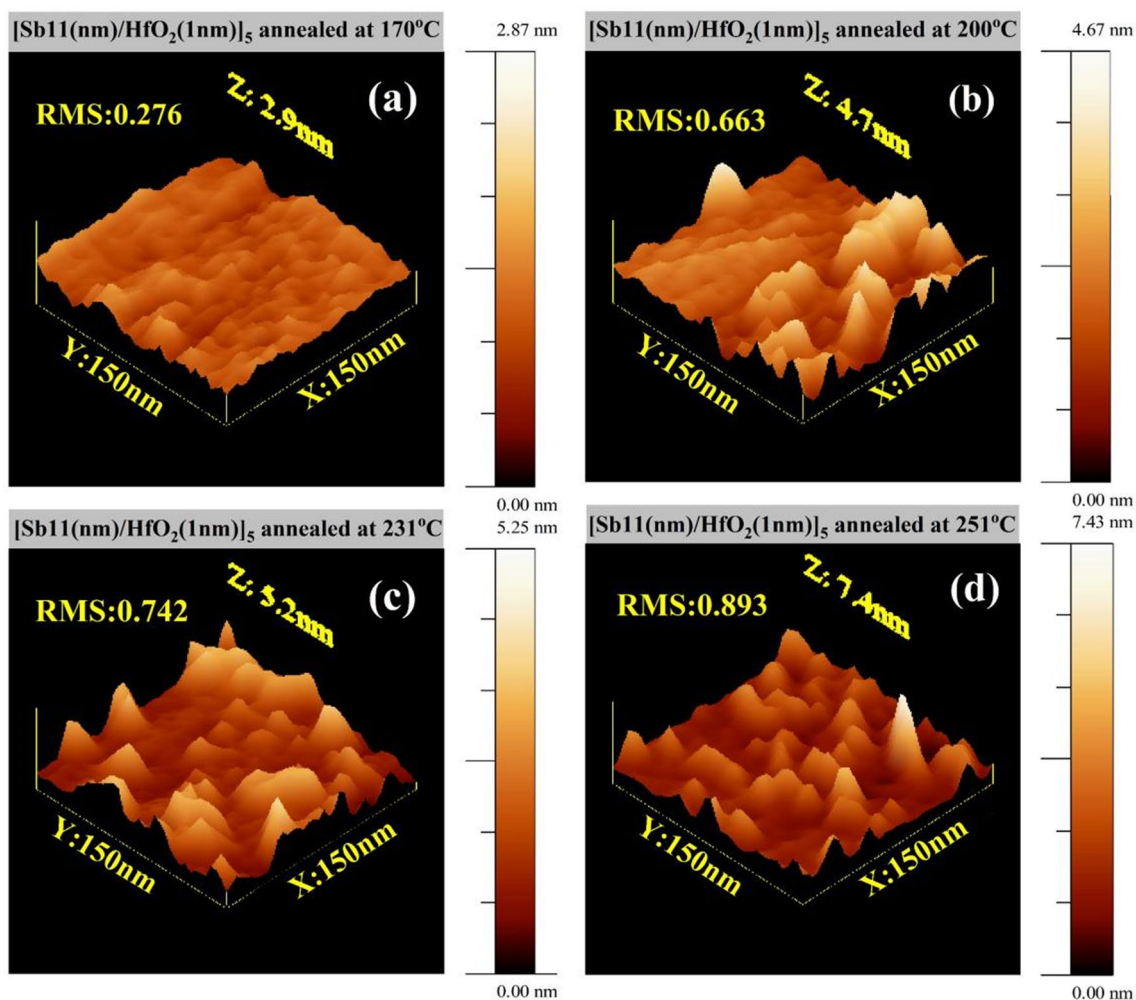

Fig. 5 **a–d** AFM topographic images of [Sb(11 nm)/HfO2(1 nm)]$_4$ multilayer thin films annealed at 170, 200, 231 and 251 °C

HfO2(1 nm)]$_4$ thin film annealed at different temperatures through the AFM measurement. The surface of the film became rougher after annealing due to the internal stress produced by endothermic transformation, which indicated that the films began to change from amorphous to crystalline state. For the [Sb(11 nm)/HfO2(1 nm)]$_4$ thin film annealed at 170 °C in Fig. 5a, the surface was smooth with the root-mean-square surface roughness (RMS) of 0.276 nm. After annealed at 200, 231 and 251 °C, the RMS increased slightly to 0.667, 0.742 and 0.893 nm, respectively. With the increase of annealing temperature, the crystallization of [Sb(11 nm)/HfO$_2$(1 nm)]$_4$ film became more obvious. The surface became rougher and the grains tended denser. In addition, the RMS of pure Sb thin film was 2.3097 nm [22]. It implied that the strain in [Sb(11 nm)/HfO$_2$(1 nm)]$_4$ film was much smaller than that of pure Sb film, which was beneficial to increase the effective contact between electrode and film. Also, it could be deduced that PCM devices based on multilayer [Sb(11 nm)/HfO$_2$(1 nm)]$_4$ would have better cycle reliability.

In order to quantitatively study the change of film thickness in the crystallization process, the XRR spectra of single-layer Sb and multilayer [Sb(11 nm)/HfO2(1 nm)]$_{17}$ films were measured. Figure 6a and c shows the XRR patterns of Sb (200 nm) and [Sb(11 nm)/HfO2(1 nm)]$_{17}$ films, respectively. It could be found that all the reflection peak of the two thin films moved toward a higher angle after crystallization, which indicated that crystalline thin film had a higher density than the amorphous one. The modified Bragg equation was used to determine the density change before and after crystallization [30]:

$$sin^2\theta_m = 2\delta + (m + \Delta m)^2 \cdot (\lambda/2t)^2, \tag{4}$$

where $\theta_m, \delta, \lambda, m$ ($m = 1, 2, 3…$) in $m + \Delta m$, and t were reflection coefficient, a constant, wavelength of Cu–Ka radiation (0.154 nm), correction and the thickness of materials, respectively. The value of Δm is 0.5, which corresponds to the smallest or largest intensity of XRR pattern for every reflection
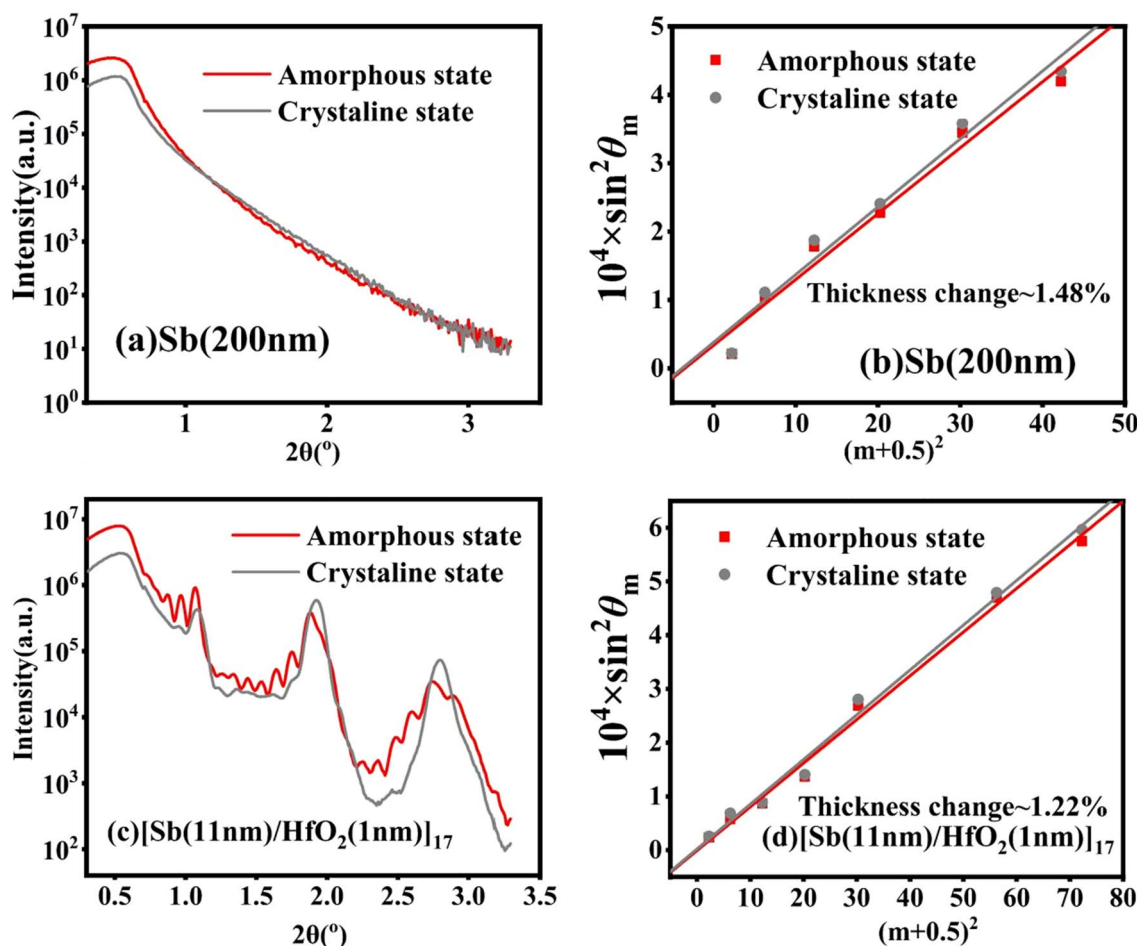

Fig. 6 XRR patterns of **a** Sb and **c** [Sb(11 nm)/HfO2(1 nm)]$_4$ films; Plots of $sin^2\theta_m$ versus $(m + \Delta m)^2$ for **b** Sb and **d** [Sb(11 nm)/HfO2(1 nm)]$_4$ films

series. Figure 6b and d exhibits the plots of $sin^2 \theta_m$ versus $(m + \Delta m)^2$. The relationship between the thickness variation of the film was calculated as [31]

$$t = \lambda/2\sqrt{k}.$$

From this, the thickness change of monolayer Sb thin film and multilayer [Sb(11 nm)/HfO2(1 nm)]$_{17}$ films before and after crystallization were calculated as 1.48% and 1.22%, respectively. The results were much smaller than the conventional GST film (-6.8%) [32]. It revealed that the existence of HfO_2 interlayers leads to a smaller thickness change, which was beneficial to the effective contact between the phase-change layer and the electrode and improved the reliability of the device. It was in accord with the results of XRD and AFM measurements.

4 Conclusions

In summary, the phase transformation properties of multilayer Sb/HfO$_2$ thin films were studied. With the decrease of the period thickness of Sb layer in Sb/HfO$_2$, the T_c increased from 154 °C of pure Sb to 239 °C of [Sb(10 nm)/HfO$_2$(1 nm)]$_5$. And the data retention temperature of 10 years increased from 127 °C of [Sb(20 nm)/HfO$_2$(1 nm)]$_3$ to 147 °C of [Sb(10 nm)/HfO$_2$(1 nm)]$_5$. In addition, the amorphous film with a relative thicker HfO$_2$ interlayer had a wider bandgap. XRD patterns revealed that HfO$_2$ layer could inhibit the crystallization of Sb making it to have a smaller grain size (5.2 nm). The RMS of [Sb(11 nm)/HfO2(1 nm)]$_4$ film annealed at 251 °C was 0.893 nm, which was much smaller than the pure Sb. The Sb/HfO$_2$ film had a smaller thickness change (-1.22%) before and after crystallization than pure Sb film (-1.48%). These results showed that HfO$_2$ interlayers could effectively inhibit the crystallization of Sb and improve the thermal stability of the composite film. Meanwhile, the smaller thickness change was beneficial to the effective contact between the phase-change layer and the electrode and improved the reliability of the device. These results demonstrated that the Sb/HfO$_2$ multilayer thin film was a promising phase-change material with high stability and reliability in PCM application.

References

1. Y. Saito, A.V. Kolobov, P. Fons, K.V. Mitrofanov, K. Makino, J. Tominaga, J. Robertson, Appl. Phys. Lett. **114**, 132102 (2019)
2. L. Wang, Z.G. Liu, C.H. Yang, J. Wen, B.S. Xiong, Appl. Phys. Express **12**, 055002 (2019)
3. H.P. You, Y.F. Hu, T.S. Lai, Q.Q. Chou, X.Q. Zhu, H. Zou, IET Nanobiotechnol. **12**, 1080–1083 (2018)
4. K.J. Huang, Y.J. Ha, R. Zhao, A. Kumar, Y. Lian, IEEE T. Circuits-I. **61**, 2605–2613 (2014)
5. Y.F. Hu, T.S. Lai, H. Zou, X.Q. Zhu, Mater. Res. Express **6**, 025907 (2019)
6. E. Palumbo, P. Zuliani, M. Borghi, R. Annunziata, Solid State Electron. **133**, 38–44 (2017)
7. M. Malvestuto, A. Caretta, B. Casarin, F. Cilento, M. Dell'Angela, D. Fausti, R. Calarco, B.J. Kooi, E. Varesi, J. Robertson, F. Parmigiani, Phys. Rev. B **94**, 094310 (2016)
8. J.G. Champlain, L.B. Ruppalt, A.C. Guyette, N. El-Hinnawy, P. Borodulin, E. Jones, R.M. Young, D. Nichols, J. Appl. Phys. **119**, 244501 (2016)
9. K.Y. Ding, K. Ren, F. Rao, Z.T. Song, L.C. Wu, B. Liu, S.L. Feng, Mater. Lett. **125**, 143–146 (2014)
10. Y.H. Zheng, Y. Cheng, M. Zhu, X.L. Ji, Q. Wang, S.N. Song, Z.T. Song, W.L. Liu, S.L. Feng, Appl. Phys. Lett. **108**, 052107 (2016)
11. Y.F. Hu, X.Q. Zhu, H. Zou, J.H. Zhang, Y. Li, J.Z. Xue, Y.X. Sui, W.H. Wu, S.N. Song, Z.T. Song, Appl. Phys. Lett. **108**, 223103 (2016)
12. X.L. Zhou, L.C. Wu, Z.T. Song, F. Rao, K. Ren, C. Peng, S.N. Song, B. Liu, L. Xu, S.L. Feng, Appl. Phys. Lett. **103**, 072114 (2013)
13. B.S. Sa, J. Zhou, Z.M. Sun, J. Tominaga, R. Ahuja, Phys. Rev. Lett. **109**, 096802 (2012)
14. P. Calka, M. Sowinska, T. Bertaud, D. Walczyk, J. Dabrowski, P. Zaumseil, C. Walczyk, A. Gloskovskii, X. Cartoixa, J. Sune, T. Schroeder, A.C.S. Appl, Mater. Inter. **6**, 5056–5060 (2014)
15. X.Q. Zhu, R. Zhang, Y.F. Hu, T.S. Lai, J.H. Zhang, H. Zou, Z.T. Song, Chinese Phys. Lett. **35**, 056803 (2018)
16. Y.F. Hu, M.C. Sun, S.N. Song, Z.T. Song, J.W. Zhai, Integr. Ferroelectr. **140**, 8–15 (2012)
17. Y. Zhu, Z. Zhang, S. Song, H. Xie, Z. Song, X. Li, L. Shen, L. Li, L. Wu, B. Liu, Mater. Res. Bull. **64**, 333–336 (2015)
18. Y.G. Lu, S.N. Song, Z.T. Song, B. Liu, J. Appl. Phys. **109**, 064503 (2011)
19. Y.G. Lu, M. Stegmaier, P. Nukala, M.A. Giambra, S. Ferrari, A. Busacca, W.H.P. Pernice, R. Agarwal, Nano Lett. **17**, 150–155 (2017)
20. H. Zou, X.Q. Zhu, Y.F. Hu, Y.X. Sui, W.H. Wu, J.Z. Xue, L. Zheng, Z.T. Song, CrystEngComm **18**, 6365–6369 (2016)
21. Z.F. He, S.Y. Chen, W.H. Wu, J.W. Zhai, S.N. Song, Z.T. Song, Appl. Phys. Express **10**, 055504 (2017)
22. X. Guo, Y.F. Hu, Q.Q. Chou, T.S. Lai, X.Q. Zhu, J. Mater. Sci-Mater. El. **29**, 16172–16177 (2018)
23. R. Zhang, Y.F. Hu, Q.Q. Chou, T.S. Lai, X.Q. Zhu, Micro. Nano Lett. **14**, 379–383 (2019)
24. F. Rao, Z.T. Song, Y. Cheng, M.J. Xia, K. Ren, L.C. Wu, B. Liu, S.L. Feng, Acta Mater. **60**, 323–328 (2012)
25. W.H. Wu, S.Y. Chen, J.W. Zhai, X.Y. Liu, T.S. Lai, S.N. Song, Z.T. Song, Appl. Phys. Lett. **110**, 181906 (2017)
26. Z.F. He, W.H. Wu, X.Y. Liu, J.W. Zhai, T.S. Lai, S.N. Song, Z.T. Song, Mater. Lett. **185**, 399–402 (2016)
27. R. Zhang, Y.F. Hu, Q.Q. Chou, T.S. Lai, X.Q. Zhu, J. Alloy. Compd. **798**, 342–349 (2019)
28. Y.F. Hu, R. Zhang, T. Lai, X.Q. Zhu, H. Zou, Z. Song, ECS J. Solid State Sc. **6**, 4 (2017)
29. H. Zou, Y.F. Hu, X.Q. Zhu, Z.T. Song, RSC Adv. **7**, 31110–31114 (2017)
30. T. Siegrist, P. Jost, H. Volker, M. Woda, P. Merkelbach, C. Schlockermann, M. Wutting, Nat. Mater. **10**, 202–208 (2011)
31. H.P. You, Y.F. Hu, X.Q. Zhu, H. Zou, S.N. Song, Z.T. Song, Appl. Phys. A-Mater. **124**, 168 (2018)
32. C.Z. Wang, J.W. Zhai, S.N. Song, Z.T. Song, M.C. Sun, B. Shen, Electrochem. Solid. St. **14**, H258–H260 (2011)